

JET PROPULSION LABORATORY

INTEROFFICE MEMORANDUM

SIM/ITP
LJAN9705151
May 15, 1997

TO: R. Laskin

FROM: L. Jandura

SUBJECT: Analysis of Hexapod Isolator Requirements Necessary to Meet SIM
OPD Requirements for Astrometry and Nulling

SUMMARY:

Three cases particularly relevant for a vibration isolation requirements study are analyzed using SIM Model v 0.0: Fringe Acquisition and Fringe Tracking for astrometry and Fringe Tracking for nulling. Two correction factors, the Model Fidelity Correction Factor and the Narrowband Correction Factor, are applied to the raw Model v 0.0 output to account for known limitations of this low fidelity model. The results show that a hexapod isolator with a 1.5 Hz corner frequency is needed to meet the SIM OPD requirements for nulling while a corner frequency of 15 Hz is sufficient for astrometry.

The large disparity in the isolation requirements between astrometry and nulling occurs because nulling requires both an extremely small rms OPD error and a very long coherent integration time. This difference is very significant as the 1.5 Hz hexapod isolator is a much greater design, implementation, and testing challenge. The 1.5 Hz isolator is certain to require a locking mechanism during launch to prevent launch loads from damaging the system. In addition, gravity offloading of this isolator during ground testing will likely be necessary. This creates additional problems with the verification of isolator performance due to coupling between the very low frequency modes of the isolator and the even lower frequency modes of the suspension system.

Distribution:

G. Blackwood

T. Livermore

M. Shao

M. Colavita

J. Marr

J. Spanos

R. Grogan

W. Mateer

R. Stoller

S. Joshi

J. Melody

J. Umland

P. Kahn

M. Milman

J. Yu

M. Levine-West

G. Neat

G. Lilienthal

Z. Rahman

Introduction

As part of the Space Interferometer Mission (SIM) and the Interferometry Technology Program (ITP), work is underway to determine what level of vibration isolation is required to enable SIM to perform its science mission in the presence of disturbances from the reaction wheels on the SIM spacecraft. This effort is part of a larger modeling and analysis effort designed to evaluate the effectiveness of all the layered vibration control technologies: active optical control, structural quieting, and vibration isolation.

This memo describes the results of analyses used to determine the level of vibration isolation needed to meet the requirements for optical pathlength difference (OPD) for SIM. Three cases are considered which represent different SIM Instrument operating modes that are particularly relevant to vibration isolation of the reaction wheel disturbance. The analysis assumes Hubble Space Telescope (HST) reaction wheels as the disturbance source and a hexapod isolator as the design solution.

Purpose of the Analysis

The analysis contained in this memo uses the SIM Model v. 0.0 to determine the hexapod isolator corner frequency needed to meet the SIM performance requirements assuming that the disturbance source is a set of four HST-class reaction wheels. Performance is analyzed during the following operating modes:

- Guide Interferometer Fringe Acquisition (Astrometry)
- Guide Interferometer Fringe Tracking (Astrometry)
- Guide Interferometer Fringe Tracking (Nulling)

Although this is not an exhaustive list of SIM Interferometer Modes of Operation, these are particularly relevant for the vibration isolation work. Table 1 lists the performance variable and its corresponding requirement for each operating mode of the interferometer considered in this analysis [1]. More detail on the definition of these operating modes is found in Appendix 6 and in another memo by the author [12]. In order to execute the Fringe Tracking operating mode for astrometry, the requirements for both Fringe Acquisition and Fringe Tracking for astrometry must be met.

The fringe blur, σ_{e_T} , is caused by the higher frequency components of OPD variation and is the relevant performance variable in each case. The coherent integration time, T_c , is the parameter needed to determine the fringe blur. The coherent integration time on the detector is one millisecond for the astrometry modes but is a much longer *one second* for nulling. The longer integration time means that much more of the low frequency OPD

Table 1: Summary of operating modes, performance variables and requirements.

Operating Mode	Performance Variable	Requirement
Fringe Acquisition (Astrometry)	<i>fringe blur</i> , σ_{e_T} ($T_c = 1ms$)	$\leq 80 \text{ nm rms}$
Fringe Tracking (Astrometry) (100 Hz BW)	<i>fringe blur</i> , σ_{e_T} ($T_c = 1ms$)	$\leq 10 \text{ nm rms}$
Fringe Tracking (Nulling) (100 Hz BW)	<i>fringe blur</i> , σ_{e_T} ($T_c = 1000ms$)	$\leq 1 \text{ nm rms}$

variation enters into the blur calculation. As will become clear in the results section, the vibration isolation performance requirements are driven by the nulling operating mode, since nulling requires both a small rms vibration level as well as long coherent integration times.

Description of the Model

This section contains a basic description of the SIM Model v 0.0 used to perform the analyses contained in this memo. Further details about the model are found in the appendices. Two correction factors, the Model Fidelity Correction Factor and the Narrowband Correction Factor, are applied to the raw Model v 0.0 output to account for limitations of the model. The first addresses the issue of model fidelity while the second deals with the issue of worst case operating conditions as they relate to the reaction wheel disturbance model.

SIM Model v 0.0

The SIM Model v 0.0 is an integrated model created using the Integrated Modeling of Optical Systems (IMOS) software package [6]. It is the lowest fidelity SIM integrated model and it is used for the purpose of conducting trade studies on the vibration isolation system. A brief summary of the model is contained in this section however more

documentation on the SIM Model v 0.0 is found in the appendices.

The structural model consists entirely of beam elements, rigid body elements, and concentrated mass and inertia elements. The siderostat and metrology booms are modeled as flexible while the optics boom is considered to be a rigid body. Nodes representing the optical elements and their masses are rigidly tied to their respective booms.

An isometric view of the structural and optics model is shown in Figure 1 (no isolator pictured). Flexible elements are shown as solid lines, rigid elements as dotted lines and nodes as circles. The simplified optical prescription is shown in yellow. Light enters the two outermost siderostat optical elements at an angle of 55 degrees above the x-y plane. (The metrology boom is 30 degrees above the x-y plane.) The light then travels parallel to the siderostat booms until it is deflected by a single switching mirror. The two beams then travel parallel to the optics boom until the beam combiner node near the bottom of the optics boom. Figure 2 is a side view of the model. This view also contains the hexapod isolator. Disturbances are injected into the model at the node in the center of the hexapod structure.

After the model is solved, structural modes higher than 1000 Hz are truncated and 0.1% damping is added to these modes. There are 49 structural modes left after truncation. The five lowest flexible structural modes are at 7.8 Hz, 8.5 Hz, 10.1 Hz, 14.6 Hz and 25.9 Hz. Cases with an isolator contain 6 additional modes. These modes are damped at 10%. The hexapod isolator bounce mode is aligned with the SIM z-axis. The reaction wheel disturbance applied is consistent with 4 reaction wheels mounted on a 4-sided, equal torque pyramid with the base of the pyramid perpendicular to the z-axis. More details about the isolator model are found in Appendix 3 while further information about the reaction wheel disturbance is found in Appendix 2. The effects of closed loop control are modeled using control filters (Appendix 7). Cases were run with no isolator, and with hexapod isolators using 20 Hz, 10 Hz, 5 Hz, 2 Hz and 1 Hz corner frequencies.

Model Fidelity Correction Factor

Low fidelity models are useful for initial system trade studies – with some reasonable engineering judgements a simple model can be created that captures the geometry, gross dynamics, and essential input-output properties of a complex system. This model can be improved to increasingly higher levels of fidelity by adding both parameter updates (to tune the system response to measured or expected lowest natural frequencies or rigid body modes) or by adding additional degrees of freedom to capture higher-frequency resonant response. Even the highest fidelity model will exhibit some degree of structured parameter error (modal frequencies, damping) or unstructured error (missing modal density at high frequencies) when compared with the actual system. The degree to which this structured or unstructured error affects the utility of a low fidelity model depends on what input-

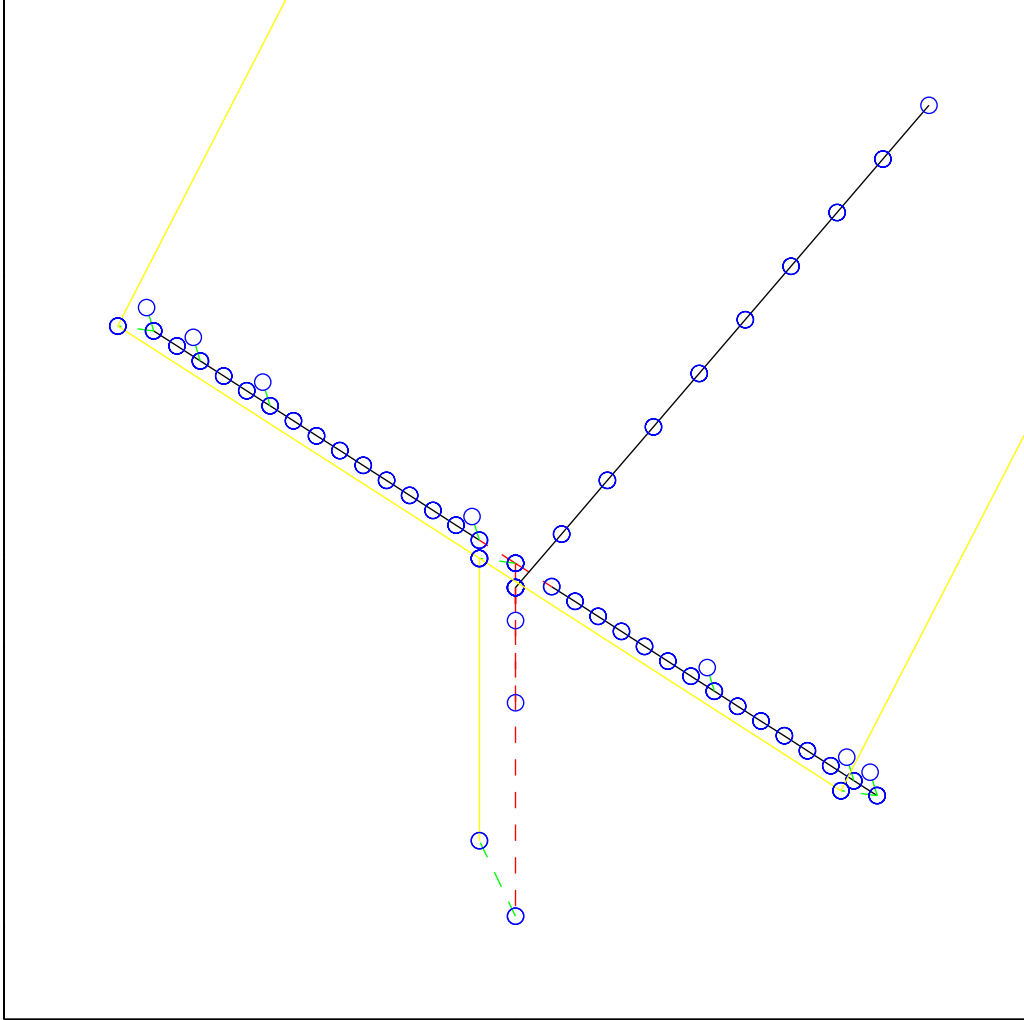


Figure 1: Isometric view of the SIM model. The solid yellow line is the stellar light path. Circles are nodes of the model which are connected with either solid lines representing flexible beam elements or with dotted lines representing rigid body elements.

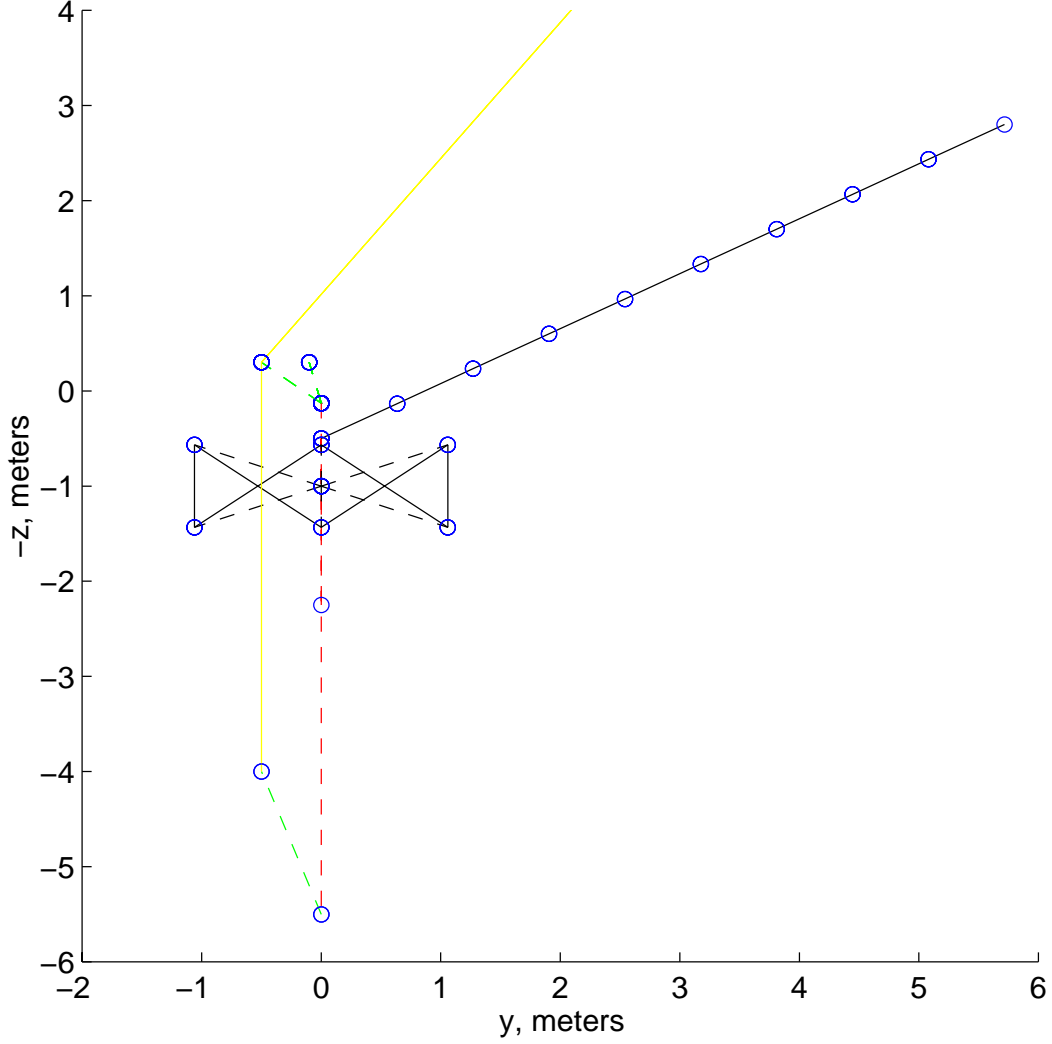


Figure 2: Side view of the SIM model. Circles are nodes of the model. Solid lines are flexible beam connections and dotted lines are rigid connections. Clearly seen in this view is the flexible metrology boom (black solid line) and the rigid optics boom (red dotted line). Stellar light (solid yellow line) enters the model at the siderostat optics node, travels along the siderostat boom (not seen in this view) and is deflected down the optics boom to the beam combiner optics node. The optics nodes are rigidly connected to the model (green dotted line). The additional node connected by the green dotted line represents the siderostat mass. The hexapod isolator is seen in black. Disturbances are injected into the model at the node in the center of the hexapod isolator.

output relationship the model is to be used for.

For vibration isolation the low fidelity model must accurately predict the energy that is transmitted from the disturbance input to the output performance metric in relatively broad energy bands (third octave bands, for example) In this case the frequency of individual modes is not nearly as important as the modal damping, and more importantly, the modal density (or number of modes per given frequency band). Modal density is important since vibration energy can be thought of as passing through many individual modal resonant pass filters – the more modes per frequency band, the more energy at the output. Thus for the isolation study it is only the structured uncertainty of modal damping and the unstructured uncertainty of missing modal density that must be considered.

To understand the nature of the unmodeled dynamics in the low fidelity SIM model, a low fidelity model of the Micro-Precision Interferometer (MPI) testbed was created with the same degree of fidelity as the low fidelity model of SIM used in this isolation study. The MPI low fidelity model was compared to the actual MPI hardware in terms of the transfer function from disturbance source to performance metric output. The Model Fidelity Correction Factor between the modeled and measured MPI plant transfer is shown in Figure 3. This frequency-dependent factor represents the scale factor that would have to be applied to the low fidelity model disturbance transfer functions so that the energy transmitted by the scaled model, for each frequency band, is identical to that for the measured plant given the same disturbance input spectrum. This work was performed by S. Joshi and more detail can be found in his documentation [2]. Joshi’s Jan 31 Model Fidelity Correction Factor is the appropriate one to use as it more accurately represents the current level of uncertainty in the SIM design. It is slightly more conservative than the Mar 19 version.

The correction factor is small at low frequencies where the low fidelity MPI model captures the beam-like behavior of the MPI measured plant. In the frequency range between 20 and 100 Hz there are component dynamics in MPI not included in the low fidelity model – namely, the 6 DOF resonances of several optical benches that support smaller components. At frequencies above 300 Hz other unmodeled dynamics result from resonances of the plate modes of optical benches and other small components. The scale factor, while developed for the MPI model, is assumed for this study to apply to the SIM low fidelity model.

Narrowband Correction Factor

The requirements specified in Table 1 must be met under all spacecraft conditions during that operating mode. While the stochastic broadband reaction wheel model gives a good indication of the nominal operating conditions, only the discrete-frequency reaction wheel model can predict the worst case operating conditions. This worst case disturbance occurs

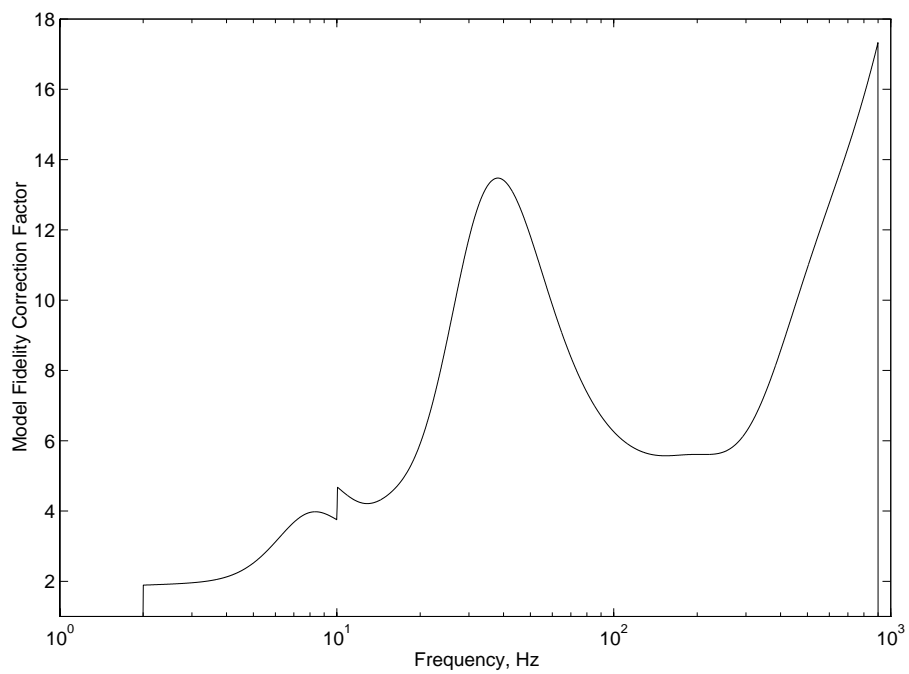


Figure 3: The Model Fidelity Correction Factor (Jan 31 version) is applied to disturbance transfer functions for PSD calculation.

when one or more of the reaction wheel harmonics aligns with one or more of the SIM modes.

MPI results [13] show that the difference in the rms OPD error between the broadband and the discrete-frequency reaction wheel disturbance model is a factor of 4.4 in the open loop case and ranges from 2.7 to 2.8 in the cases with active optical control (4-RW disturbance). A factor of 3 is used in these analyses as the Narrowband Correction Factor to account for the worst case operating conditions. Unlike the frequency-dependent Model Fidelity Correction Factor which is applied to the 6 disturbance transfer functions, this scalar correction is applied directly to the rms value.

Results from the Model

Model results are presented for the 3 operating modes and their corresponding requirements outlined in Table 1. In addition, some open loop results are provided as a basis of comparison for the controlled cases shown in later figures.

Figure 4 shows the open loop results. No blur filter is applied to these results. Notice that the worst case here is not the No Isolation case but the 20 Hz Isolation case. This occurs because the benefit gained in the higher frequencies through the disturbance attenuation of the isolator is not sufficient to offset the additional error caused by the isolator modes. This can also be clearly seen in Table 2 which shows the OPD error in each frequency band. As the isolation corner frequency decreases, additional attenuation is achieved in the middle to high frequency range and this effect clearly overwhelms any additional errors introduced by isolator modes.

The effect of the Model Fidelity Correction Factor is also seen in the table. In the No Isolation case, the rms OPD error is increased by a factor of 4.85 over the 1-1000 Hz frequency range. The smallest correction is a factor of 4 in the 1-10 Hz frequency band and the largest is 5.7 in the 100-1000 Hz range. The difference in rms OPD error in the 10-100 Hz frequencies is a factor of 4.8.

The fringe acquisition results for astrometry are shown in Figure 5. The 20 Hz isolator is not quite sufficient to meet the 80 nm rms requirement however the 10 Hz isolator easily meets the requirement. It is likely that an isolator in the 15-18 Hz range would also satisfy the requirement but since the relationship is not linear, the actual cases would have to be calculated in order to verify this supposition.

Fringe tracking results for astrometry are in Figure 6. Table 3 shows the OPD error by frequency band for this operating mode. In this case the 10 Hz isolator easily meets the 10 nm rms requirement and it is likely that a 15 Hz isolator would also be sufficient. This astrometry operating mode is a slightly more difficult case for isolation than the fringe acquisition mode and therefore it drives the isolator requirements for astrometry.

The requirements for nulling clearly present the most difficult case for vibration isola-

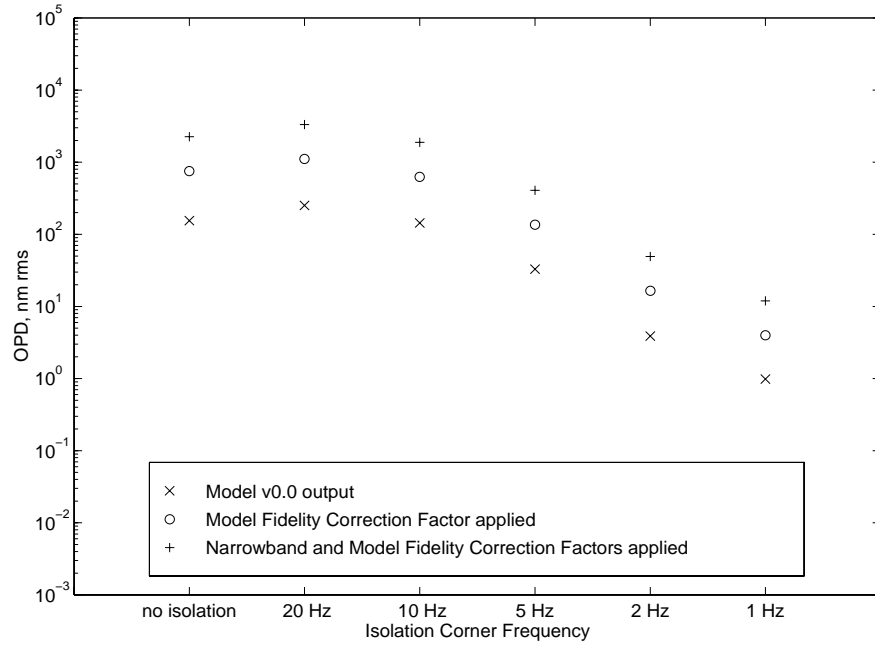


Figure 4: Open loop OPD versus isolation corner frequency.

Table 2: Distribution of open loop OPD by frequency.

		OPD Error, nm rms			
		1-1000 Hz	1-10 Hz	10-100 Hz	100-1000 Hz
No Isolation	Model v0.0 output	154.91	30.81	146.34	40.42
	Model Fidelity Corrected output	750.99	121.36	704.39	230.43
20 Hz Isolation	Model v0.0 output	252.17	35.41	249.66	2.40
	Model Fidelity Corrected output	1113.90	139.46	1105.10	13.49
10 Hz Isolation	Model v0.0 output	143.74	67.50	126.90	0.60
	Model Fidelity Corrected output	628.53	265.80	569.50	3.20
5 Hz Isolation	Model v0.0 output	32.92	26.14	20.02	0.14
	Model Fidelity Corrected output	136.39	103.00	89.40	0.80
2 Hz Isolation	Model v0.0 output	3.89	2.66	2.84	0.03
	Model Fidelity Corrected output	16.36	10.33	12.69	0.19
1 Hz Isolation	Model v0.0 output	0.98	0.69	0.70	0.02
	Model Fidelity Corrected output	3.98	2.39	3.18	0.13

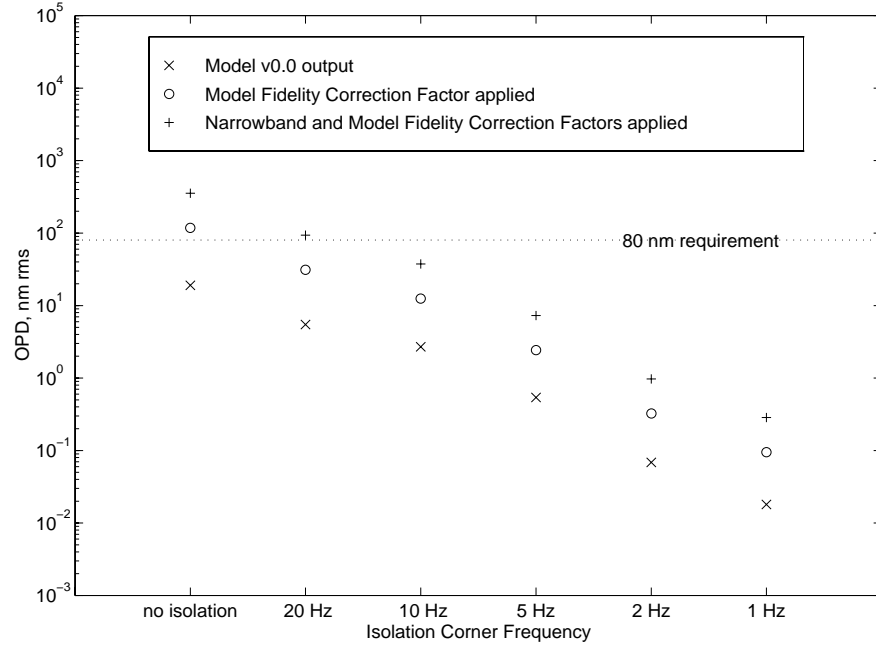


Figure 5: Fringe acquisition OPD versus isolation corner frequency.

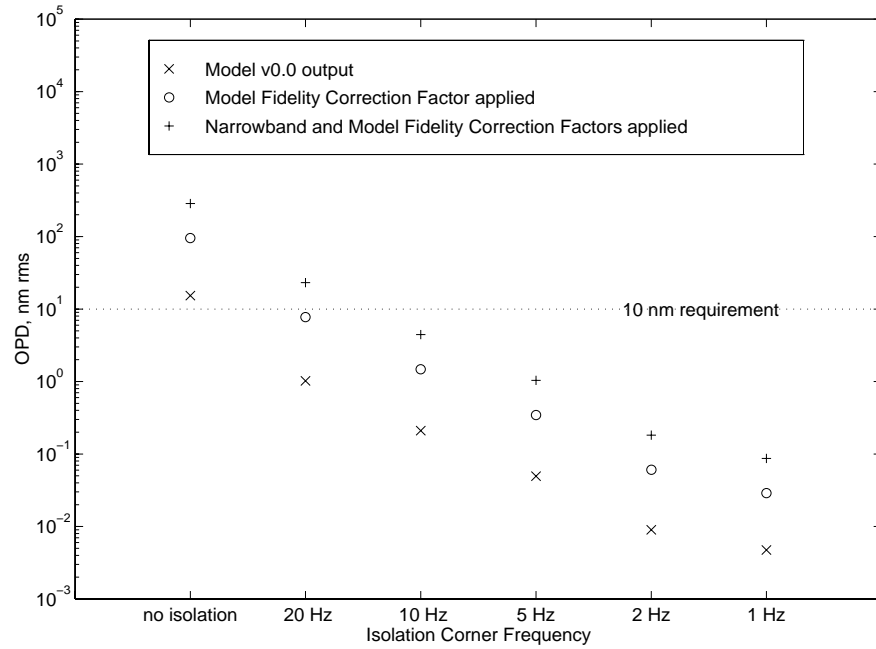


Figure 6: Fringe tracking (astrometry) OPD versus isolation corner frequency.

Table 3: Distribution of fringe tracking (astrometry) OPD by frequency. (Numbers are rounded to 2 decimal places. Numbers smaller than 0.005 nm are recorded as 0.00.)

		OPD Error, nm rms			
		1-1000 Hz	1-10 Hz	10-100 Hz	100-1000 Hz
No Isolation	Model v0.0 output	15.27	0.00	1.20	15.22
	Model Fidelity Corrected output	95.16	0.01	10.79	94.55
20 Hz Isolation	Model v0.0 output	1.02	0.00	0.79	0.64
	Model Fidelity Corrected output	7.71	0.01	6.82	3.59
10 Hz Isolation	Model v0.0 output	0.21	0.01	0.15	0.15
	Model Fidelity Corrected output	1.48	0.02	1.22	0.84
5 Hz Isolation	Model v0.0 output	0.05	0.00	0.03	0.04
	Model Fidelity Corrected output	0.35	0.01	0.27	0.21
2 Hz Isolation	Model v0.0 output	0.01	0.00	0.01	0.01
	Model Fidelity Corrected output	0.06	0.00	0.04	0.04
1 Hz Isolation	Model v0.0 output	0.00	0.00	0.00	0.00
	Model Fidelity Corrected output	0.03	0.00	0.01	0.02

tion. The fringe tracking results for nulling in Figure 7 indicate that a 1-1.5 Hz hexapod isolator is necessary to achieve the 1 nm rms requirement. It is the combination of both a small rms OPD error as well as a long coherent integration time that makes this case so difficult.

Intermediate Model Results

In order to more fully understand the effects of the different model components on the result, we will trace the development of the results for the case of 100 Hz Guide Fringe Tracking with 10 Hz isolation found in Figure 6. These intermediate results clarify the effects of active control, isolation, the blur filter, and the Model Fidelity Correction Factor on the model results.

Figure 8 shows the disturbance transfer functions which quantify the effect on OPD from a force in the x-direction. The open loop case (OL) is the worst case. Adding an isolator but no active optics (OL, 10 Hz isolation) improves performance by attenuating high frequency disturbances. Adding active optics but no isolation (100 Hz FT) improves the low frequency performance. In Figure 9, the effect of both active optics and isolation are shown (100 Hz FT, 10 Hz isolation). This gives both low and high frequency performance improvement with little effect on the middle frequencies. The Model Fidelity Correction Factor raises the level of the disturbance transfer function throughout all the frequencies with the largest effect at the higher frequencies. There are 6 disturbance transfer func-

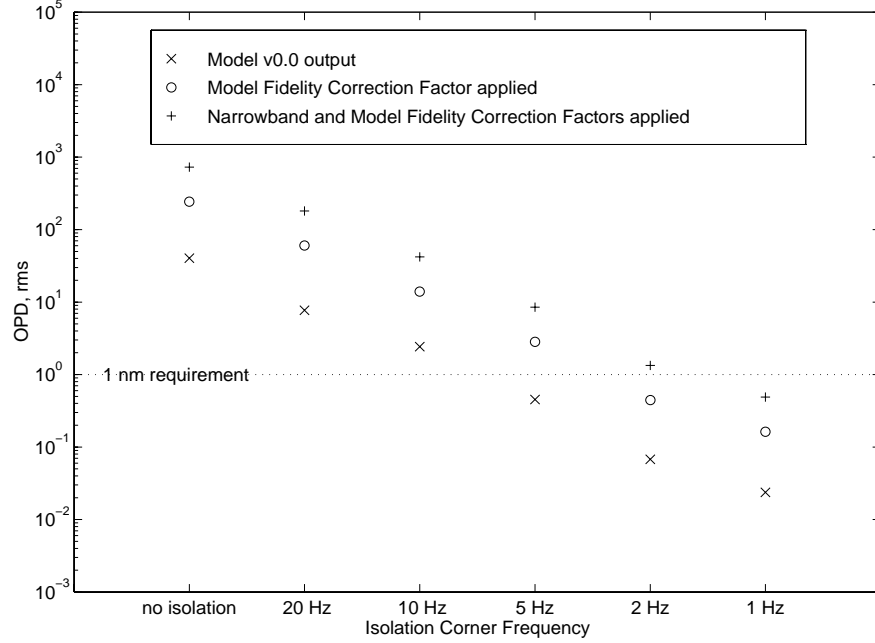


Figure 7: Fringe tracking (nulling) OPD versus isolation corner frequency.

tions corresponding to the 6 spacecraft degrees of freedom which each demonstrate the same effects as those described above for the case of an x-axis force.

The power spectral densities for total OPD error caused by a 4-RW disturbance input predictably show the same trends as the disturbance transfer functions for the effects of active optical control, isolation, and the Model Fidelity Correction Factor. In Figure 10, the open loop power spectral density (OL) is once again the worst case, contributing OPD error across the entire frequency spectra. Adding an isolator but no active optics (OL, 10 Hz isolation) removes much of the error in the high frequency region. The degree of attenuation varies with the corner frequency of the isolation. Adding active optics but no isolation (100 Hz FT) removes most of the low frequency OPD error. In Figure 11, the effect of both active optics and isolation (100 Hz FT, 10 Hz isolation) combine to remove OPD error at both the low and high frequency bands with little effect on the middle frequencies. Applying the Model Fidelity Correction Factor to the disturbance transfer functions causes the level of the power spectral density to increase throughout all the frequencies with the largest effect at the higher frequencies.

Figure 12 illustrates the effect of the 1 ms blur filter. The OPD error below the 1 kHz detector sampling frequency is significantly attenuated by the blur filter, particularly at frequencies below 100 Hz. In the case where the Model Fidelity Correction Factor is applied (Figure 13), the level of the power spectral density is raised across all frequencies.

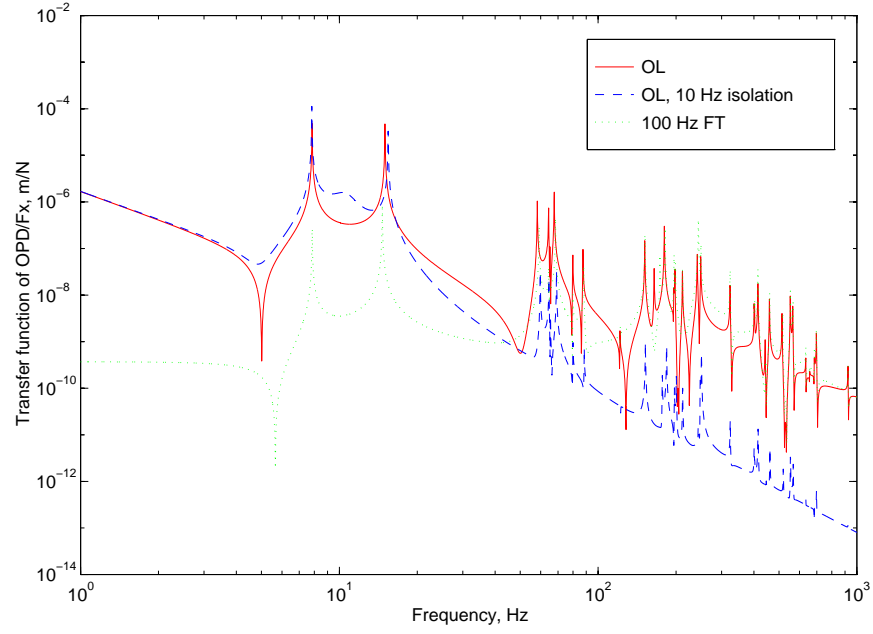


Figure 8: The OPD/Fx transfer function for 3 different cases (open loop; 10 Hz isolation; and 100 Hz FT).

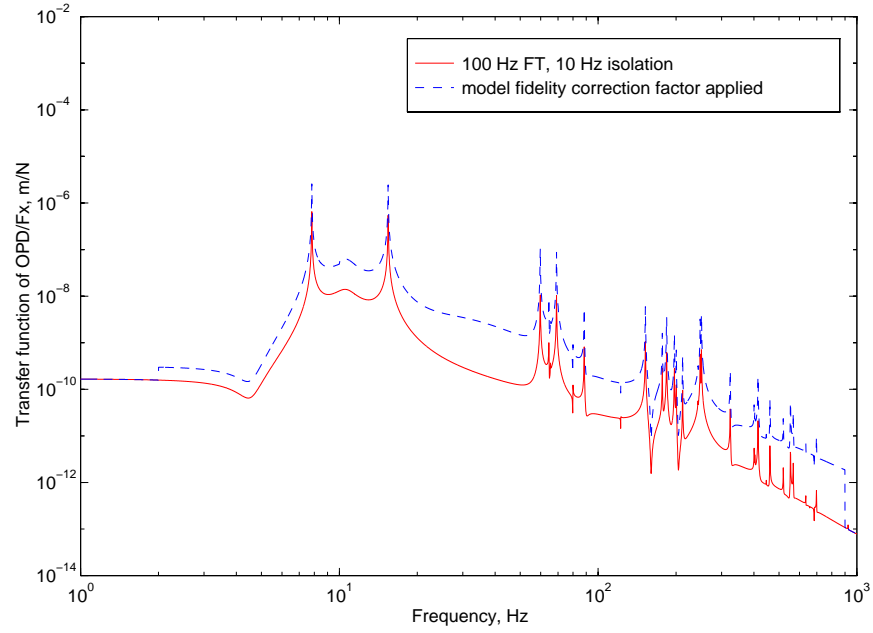


Figure 9: The OPD/Fx transfer function (100 Hz FT, 10 Hz isolation) with and without the Model Fidelity Correction Factor.

The integrated area under these two power spectral densities represents the rms OPD error for each case. These two values are plotted in Figure 6 as the Model v 0.0 output data point and the Model Fidelity Correction Factor applied data point for the 10 Hz Isolation Corner Frequency case.

Conclusions

This analysis indicates that a hexapod isolator with a 15 Hz corner frequency is sufficient to meet the OPD requirements defined for astrometry. However the nulling requirements necessitate a much softer hexapod isolator with a 1.5 Hz corner frequency. The large disparity in the isolation needs for the two different operating modes occurs because nulling requires both an extremely small rms OPD error and a very long coherent integration time.

There are big differences between 15 Hz and 1.5 Hz in terms of the isolation hardware. Isolation systems around 10 Hz or less often require launch locks due to dynamic excursions during launch. Isolators around 10 Hz are usually stiff enough to make ground testing relatively easy while isolators in the 1-2 Hz region create much more difficulty. A passive, 1-2 Hz isolator typically needs gravity offloading during ground testing but this adds the additional problem of coupling between the suspension modes and the isolator modes making isolator performance difficult to verify. For these reasons active isolation is often an attractive solution in the 1-2 Hz isolator range. Future analysis of isolator transmissibility requirements will help clarify whether an active or passive system is needed to meet SIM nulling requirements.

It is appropriate to mention some caveats about the analysis presented here. Although SIM Model v 0.0 was corrected for known weaknesses through the use of the Model Fidelity and the Narrowband Correction Factors, *no additional design margin* was assumed in establishing the requirements for the hexapod isolator. However the 0.1% damping used for the structural modes is probably very low. The actual structural damping experienced in space may be a factor of 3 or more higher. The conservative assumption concerning structural damping may in fact substitute for an explicit design margin in the analysis.

This analysis presents the requirements for a hexapod isolator point design which will meet the SIM OPD requirements for the cases of astrometry and nulling. In the future the isolator geometry could be optimized for the directionality of the disturbance but the corner frequency, particularly for the principal disturbance direction, is unlikely to change much from the results presented here.

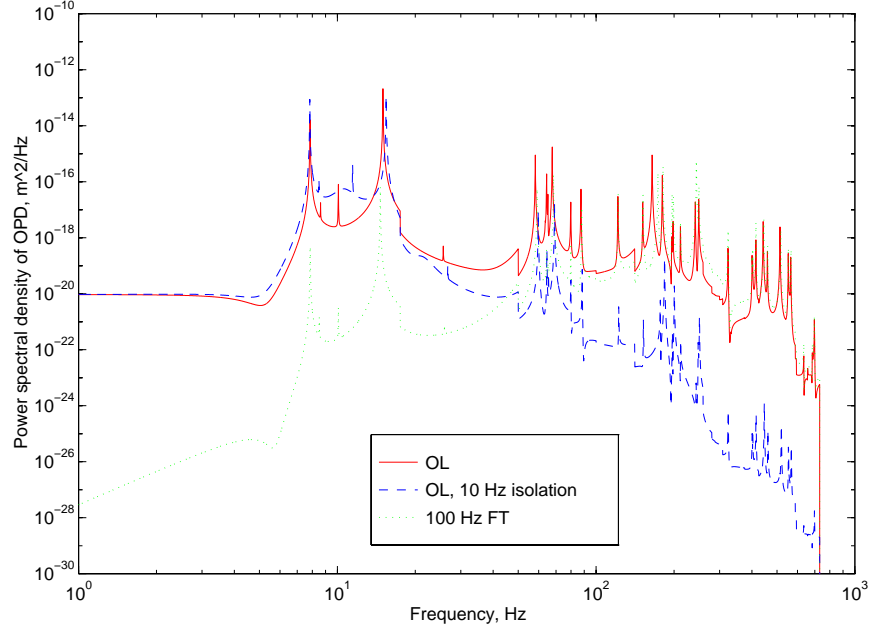


Figure 10: The power spectral density of total OPD error for a 4-RW disturbance. Three cases are shown (open loop; 10 Hz isolation; and 100 Hz FT).

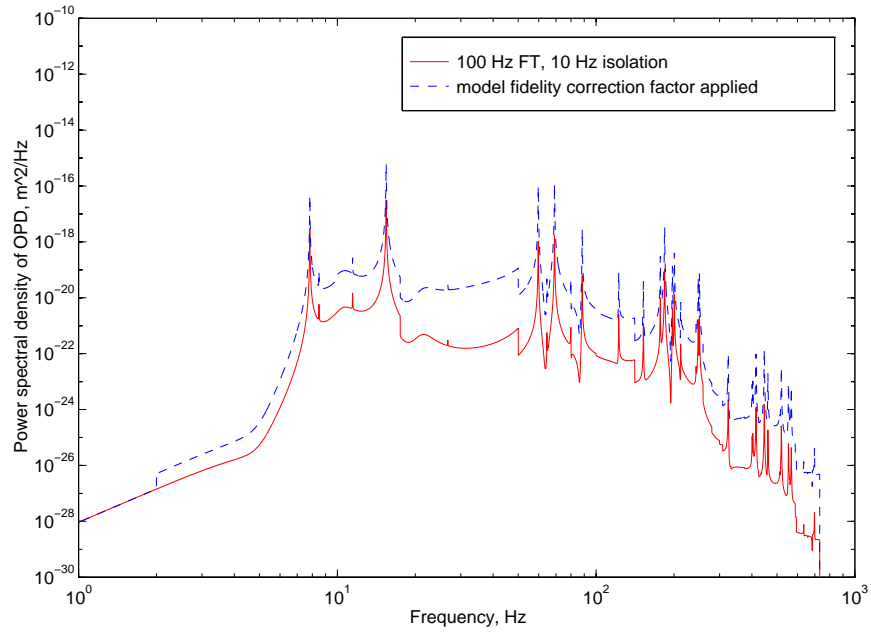


Figure 11: The power spectral density (100 Hz FT, 10 Hz isolation) of total OPD error for a 4-RW disturbance, with and without the Model Fidelity Correction Factor.

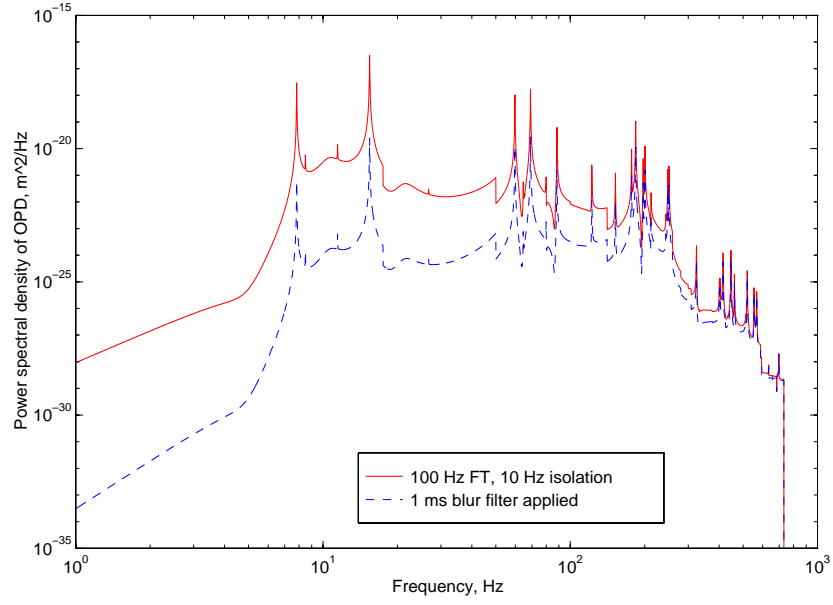


Figure 12: The power spectral density (100 Hz FT, 10 Hz isolation) of total OPD error for a 4-RW disturbance, with and without the 1 ms blur filter.

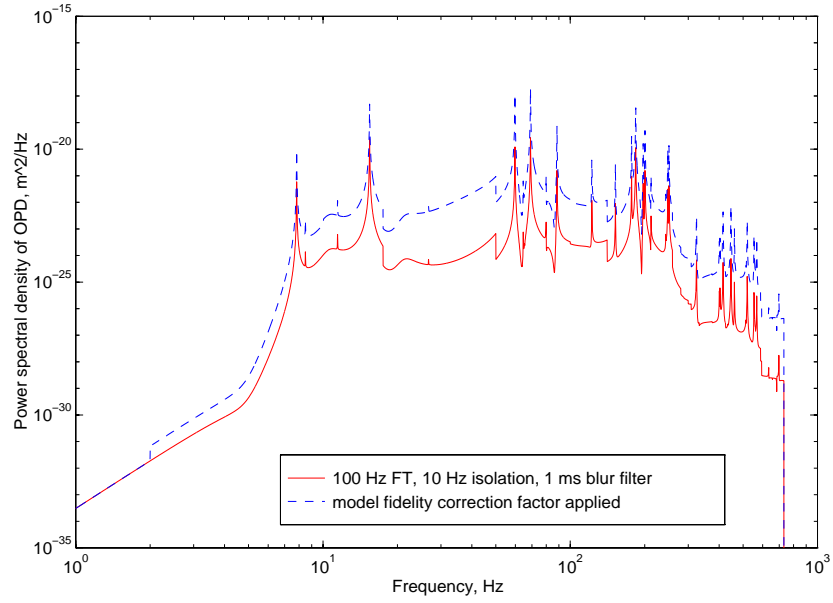


Figure 13: The power spectral density (100 Hz FT, 10 Hz isolation, 1 ms blur filter) of total OPD error for a 4-RW disturbance, with and without the Model Fidelity Correction Factor.

Appendix 1: Definition of SIM IMOS Model v 0.0 and SIM IMOS Model v J1.0

Understanding the performance requirements for the Vibration Isolation Subsystem requires an understanding of the overall spacecraft implementation and performance particularly in the areas of the spacecraft structure, the optics layout, the spacecraft and component control systems, the disturbance source, and the performance metrics. The general modeling approach taken for the purpose of specifying the Vibration Isolation Subsystem requirements is to start with the lowest fidelity model deemed technically useful in each of the areas, adding increasing fidelity as necessary as our knowledge of this specific vibration isolation problem and the overall SIM spacecraft design matures. Each of the SIM integrated models contains the following subcomponents: Disturbance Analysis Method, Reaction Wheel Assembly (RWA) Model, Isolation Model, Structural Model, Optics Model, Output Performance Metric, and Closed Loop Synthesis.

Table 4 defines the level of model fidelity used for each component of the two lowest fidelity integrated SIM models, Model v 0.0 developed by L. Jandura and Model v J1.0 developed by J. Melody. Two parts of Model v 0.0, the RWA Model and the Isolation Model, were upgraded to the higher fidelity version described under Model v J1.0. This was done when the lower fidelity versions proved an inadequate match to the rest of the model components, particularly the Structural Model and the Optics Model. Details of all of the Model v 0.0 components are found in the appendices that follow.

Model v 0.0 contains a single baseline stellar interferometer with a simplified optical prescription. Light is modeled as entering the siderostats at an angle of 55 degrees above the xy-plane from the positive y-axis side of the spacecraft (the same side as the metrology boom). The optical prescription includes only the two outermost siderostats, a single switching mirror and a single beam combiner. These optics are mounted on a low-order, IMOS beam element model. The siderostat and metrology booms are modeled as flexible while the optics boom is modeled as a rigid body. Nodes representing the optical elements and their masses are rigidly tied to their respective booms. Dynamically uncoupled filters represent the control system effects. The original definition of Model v 0.0 included only a one-wheel, two-axis (one force and one torque) reaction wheel disturbance and a corresponding two-axis isolation model. This was changed to a one-wheel, five-axis (three forces and two torques) reaction wheel disturbance and a corresponding six-axis isolation model to ensure that all modes of the three-dimensional structural and optics models were excited by the disturbance source. The broadband reaction wheel disturbance model is used. The torque disturbance was further upgraded to a four-wheel, six-axis (three forces and three torques) for the purpose of developing isolation requirements. Optical pathlength difference (OPD) is the only optical performance metric considered.

Model v J1.0 also contains a single baseline stellar interferometer but adds internal

metrology. Light enters the siderostats from the same direction as in Model v 0.0. The more complicated optical prescription also includes all seven of the siderostats, a single switching mirror and a single beam combiner. In addition, it has two beam compressors, two fast steering mirrors, one active delay line and one passive delay line. These optics are mounted on the same low-order, IMOS beam element model, modified to include additional flexible elements to capture the delay line and fast steering mirror dynamics. Actual control loops are closed on the open loop plant and sensor noise is modeled. The disturbance source is a one-wheel, five-axis (three forces and two torques) reaction wheel disturbance used in conjunction with the discrete-frequency reaction wheel disturbance model. Both OPD and wavefront tilt (WFT) are considered as performance metrics. Six-axis isolation is included.

Table 4: Definition of SIM Model v 0.0 and SIM Model v J1.0.

	Model v 0.0 (Louise)	Model v J1.0 (Jim)
A. DISTURBANCE ANALYSIS METHOD	Stochastic broadband reaction wheel disturbance model (Reference IOM 3411-95-200csi by J. Melody)	Discrete-frequency reaction wheel disturbance model <ul style="list-style-type: none"> • Sweep over wheel speeds (Reference same Melody IOM)
B. RWA MODEL	Hubble Space Telescope harmonic disturbance model <ul style="list-style-type: none"> • One-wheel, two-axis disturbance (one force, one torque) 	Hubble Space Telescope harmonic disturbance model <ul style="list-style-type: none"> • One-wheel, five-axis disturbance (three forces, two torques)
C. ISOLATION MODEL	Two-axis isolation <ul style="list-style-type: none"> • Two-parameter model for each axis (one spring, one damper) • Assume proportional damping • Dynamic coupling (isolator springs and masses included as part of structural model) 	Six-axis isolation <ul style="list-style-type: none"> • Two-parameter model for each axis (one spring, one damper) • Assume proportional damping • Dynamic coupling (isolator springs and masses included as part of structural model)
D. STRUCTURAL MODEL	Low-order, beam-like IMOS model <ul style="list-style-type: none"> • Composed of beams, rigid body elements, and nodes for the optical elements • Siderostat boom and metrology boom modeled as flexible • Optics boom modeled as rigid • Booms tied rigidly to each other • Nodes for optical elements tied rigidly to each respective boom 	All characteristics of Model v 0.0 plus: <ul style="list-style-type: none"> • Additional structural dynamics (i.e. flexible elements) to model optical delay lines and fast steering mirrors
E. OPTICS MODEL	One baseline, stellar interferometer Simplified optical prescription includes: <ul style="list-style-type: none"> • siderostats • beam combiner Create optical C-matrix by hand (i.e., not using COMP)	One baseline, stellar interferometer and internal metrology Detailed optical prescription includes: <ul style="list-style-type: none"> • siderostats • beam combiner • optical delay lines (one active, one passive) • fast steering mirrors Use COMP to create optical C-matrix
F. OUTPUT PERFORMANCE METRIC	Definition of SIM optical performance metrics and relevant operation modes as compatible with low fidelity model <ul style="list-style-type: none"> • OPD only 	Definition of SIM optical performance metrics and relevant operation modes as compatible with low fidelity model <ul style="list-style-type: none"> • OPD and WFT
G. CLOSED LOOP SYNTHESIS	Use dynamically uncoupled filter to represent control loop attenuation ($1/(1 + \text{loop gain})$) <ul style="list-style-type: none"> • BW limits from rules of thumb • Control sensor noise not modeled 	Actually close control loops on the open loop plant (capture the dynamic coupling) <ul style="list-style-type: none"> • Model sensor noise

Appendix 2: Disturbance Analysis Method and RWA Model

Two models of reaction wheel disturbance forces and torques based upon testing of the Hubble Space Telescope (HST) reaction wheels are available [10]. In the discrete-frequency reaction wheel disturbance model, the disturbances are modeled as sinusoidal components at harmonic frequencies of the reaction wheel speed. A stochastic broadband reaction wheel disturbance model was created from the discrete-frequency model by assuming that the reaction wheel speed is a uniform random variable over some wheel speed interval. The broadband model more easily lends itself to frequency domain analysis and control design.

The models represent disturbance forces in the plane of the wheel or radial forces, disturbance forces along the spin axis of the wheel or axial forces and disturbance torques about axes in the plane of the wheel or radial torques. Variations in torque about the axis of rotation were negligible. Disturbances from a single reaction wheel are modeled using two radial forces, one axial force, and two radial torques. Additional reaction wheels are modeled by adding another set of five disturbance forces/torques for each wheel.

Figure 14 shows the power spectral densities of a radial disturbance force, an axial disturbance force, and a radial disturbance torque assuming that the reaction wheel speed is a uniform distribution from 0 to 3000 rpm.

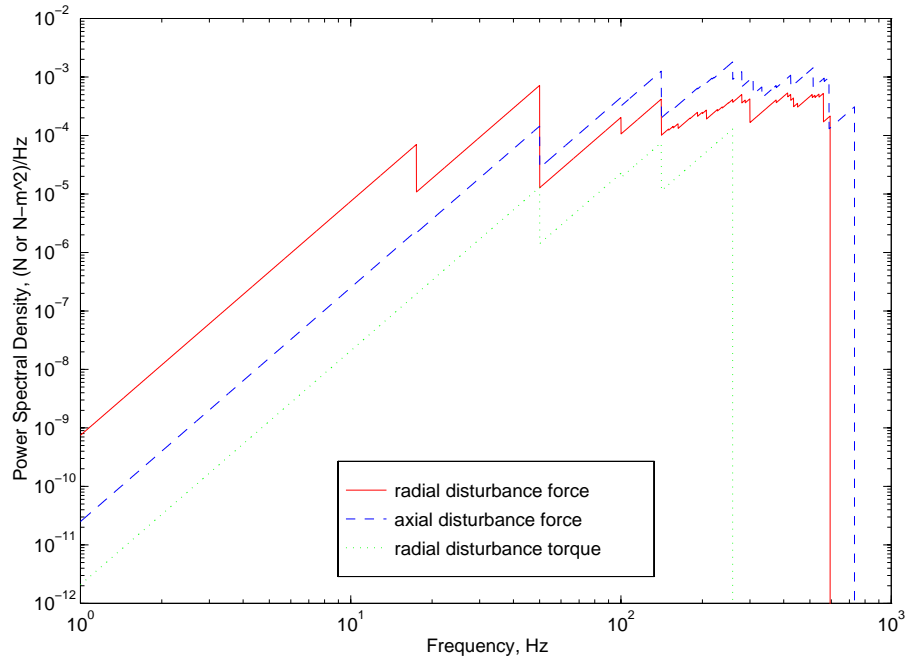


Figure 14: Power spectral densities of the disturbance forces and torques from the broadband reaction wheel model assuming a uniform distribution of wheel speeds from 0 to 3000 rpm.

Table 5: Modal frequencies of the hexapod isolator by itself and when coupled to the entire structural model.

		Hexapod Isolator Modal Frequencies, Hz					
20 Hz Isolator	Uncoupled Modes	19.64	19.64	20.00	20.00	20.00	42.43
	Coupled Modes	19.74	20.02	20.38	21.63	21.65	40.99
10 Hz Isolator	Uncoupled Modes	9.82	9.82	10.00	10.00	10.00	21.21
	Coupled Modes	9.51	9.80	10.01	10.58	10.62	21.20
5 Hz Isolator	Uncoupled Modes	4.91	4.91	5.0	5.0	5.0	10.61
	Coupled Modes	4.93	4.94	5.27	5.29	5.29	10.67
2 Hz Isolator	Uncoupled Modes	1.96	1.96	2.00	2.00	2.00	4.24
	Coupled Modes	1.97	1.98	2.12	2.12	2.12	4.26
1 Hz Isolator	Uncoupled Modes	0.98	0.98	1.00	1.00	1.00	2.12
	Coupled Modes	0.99	0.99	1.06	1.06	1.06	2.13

Appendix 3: Isolation Model

The isolation model is an orthogonal hexapod isolator as described in presentations by K. Smith and J. Spanos, et al. [3, 4]. The isolator is made of six-identical struts arranged in a hexapod configuration between a base plate which is connected to the spacecraft and a payload plate. Given that the six struts have equal stiffness, the stiffness matrix of the isolator is diagonal. If the payload mass matrix is also diagonal then the six natural frequencies of the isolator are identical. Deviations from this ideal payload cause a spread in the natural frequencies. One cause of this deviation are offsets of the payload center of gravity from the hexapod center while another is related to the payload moments of inertia. When this occurs, the translational frequencies remain the same but the bending and torsional frequencies change. Once connected to the spacecraft structure, the isolator modal frequencies shift around further due to coupling with the spacecraft structure. Table 5 shows both the uncoupled and coupled modes of the hexapod isolator used in Model v 0.0. 10% damping is added to the isolator modes.

Appendix 4: Structural Model

This section describes both the Model v 0.0 configuration and its parameters. The configuration is an integral part of the model and as such is not meant to be changed. Changes in the configuration of the model correspond to increases in its fidelity and are meant to capture increasingly fine details in the SIM spacecraft. The parameters of the model however are meant to be changed as necessary to do trade studies or to reflect the current understanding of the SIM spacecraft as its design develops. The parameters presented below reflect the best current understanding of the spacecraft design.

Configuration

The Model v 0.0 structural model is an IMOS model consisting solely of beam elements, rigid body elements (rbe2) and concentrated mass and inertia elements (conm). The siderostat and metrology booms are modeled as flexible while the optics boom is modeled as a rigid body. Nodes representing the optical elements and their masses are rigidly tied to their respective booms. Figures 1 and 2 show isometric and side views of the model nodes, connectivity and configuration. The rigidly connected optics boom (indicated by the dotted lines) consists of seven nodes: one at the intersection of the siderostat boom and the optics boom, one each at the beginnings of the positive-x and negative-x portions of the siderostat boom, one at the beginning of the metrology boom, one for the end of the optics boom, one for the optics boom mass properties and one to introduce disturbances and build the vibration isolator. In addition, there are two optics nodes rigidly attached to the optics boom: a node for the beam combiner attached to the end of the optics boom and a node for a single switching mirror attached to the node at the intersection of the optics boom and the siderostat boom. The positive-x and negative-x portions of the siderostat boom and the metrology boom are modeled as flexible. The number of nodes contained in each of these three flexible booms is variable and is chosen as a parameter of the model. An optics node representing the center of the siderostat mirror is rigidly connected to the node on the end of each siderostat boom. These optically model only a single siderostat pair representing the largest baseline of the interferometer. Nodes are added to the siderostat booms to model the mass centers for all of the siderostat bays. These nodes are cantilevered off of the nearest siderostat boom node in the x-direction. Only the mass of a siderostat bay (no inertia properties) is added to each of these nodes. Mass (no inertia properties) is also added to the end node of the metrology boom to represent the metrology structure and beam launchers at the end of the boom.

Parameters

The interferometer baseline, defined as the distance between the centers of the outermost siderostat mirrors, is 10 meters. The parameters for all three flexible booms, the positive-x siderostat boom, the negative-x siderostat boom, and the metrology boom, are chosen to produce a 5-Hz first bending mode for each boom when modeled as a clamped-free, single-span beam with the fixed end defined as the attachment to the optics boom. The siderostat booms are box beam sections, 0.95 meters by 0.26 meters and 3 millimeters thick. The length of one boom from where it attaches to the optics boom to the end is 4.75 meters, the end siderostat attaches at 4.5 meters. High modulus graphite was chosen as the material to meet the desire that the CTE of the material be less than 1 ppm. The following material properties are consistent with high modulus graphite and are used for the siderostat-boom, beam elements.

- elastic modulus, $E = 103 \times 10^9 Pa$
- density, $\rho = 1656 \frac{kg}{m^3}$
- shear modulus, $G = 1.379 \times 10^{10} Pa$
- torsional moment of inertia, $J = 2.93 \times 10^{-4} m^4$

The mass of a siderostat bay is 50 kg. Using a clamped-free, single-span beam model (i.e. the usual cantilever beam clamped at one end) and assuming that the mass of 3 siderostat bays plus the beam mass is all at the end of the beam (a conservative choice) gives the frequencies: 6.65 Hz in the less stiff bending direction and 18.13 Hz in the more stiff bending direction which meets the desired 5 Hz requirement so these parameters will do for now.

The metrology boom is 6.6 meters in length. The mass of structure including the boom and the metrology structure on the end is 55 kg with an additional 28 kg of beam launchers mounted on the metrology structure. Of the 55 kg, 50 kg is uniformly distributed along the beam and 5 kg is the metrology structure at the end. Since no other information exists at this time, this boom was modeled as a hollow cylinder with a radius of 0.1524 meters and a thickness of 3 mm. Material properties consistent with aluminum were initially chosen and iterated until both the mass distribution and the bending frequency requirements were satisfied. The final mass properties chosen are the following.

- elastic modulus, $E = 2.5 \times 10^{11} Pa$
- density, $\rho = 2.7 \times 10^3 \frac{kg}{m^3}$
- shear modulus, $G = \frac{E}{2(1+0.3)} = 9.6 \times 10^{10} Pa$

Again making the conservative assumption of lumping all the mass at the end of the beam gives a frequency of 5.12 Hz that satisfies the requirement.

The optics boom is a 1 meter by 1 meter box beam with a length of 5.5 meters. It is assumed to be a rigid body of mass 1200 kg. Inertia properties are calculated with the assumption that all the mass is evenly distributed throughout the optics boom volume.

Appendix 5: Optics Model

The stellar light path which describes the simplified optical prescription contained in SIM Model v 0.0 is shown in Figure 1. Stellar light enters the two outermost siderostats from an angle of 55 degrees above the x-y plane. The light then travels parallel to the siderostat booms and inward toward a single switching mirror located near the intersection of the siderostat and optics booms. After reaching the switching mirror, both beams travel parallel to the optics boom to the beam combiner.

In order to combine the optical prescription with the structural finite element model, a linear optical model of the form:

$$OPD = C_{opt}d \quad (1)$$

is created where d is a vector of the six optical element position and orientation perturbations for each element in the optical prescription, C_{opt} is the optical sensitivity matrix, and OPD is optical pathlength difference, the desired optical output. The block diagrams and equations in Appendix 6 require the set of disturbance transfer functions from each of the six disturbance force/torque directions at the input disturbance node (the reaction wheel location) to the OPD output for the cases of total OPD error, external OPD error, and internal OPD error. The external OPD error is the OPD error in the path from the star to the siderostats while the internal OPD error is the OPD error in the path from the siderostats to the beam combiner. The optical sensitivity matrices for these three cases follow [14].

The optical sensitivity matrices for total OPD error are:

$$\begin{aligned} S+ &= \begin{bmatrix} 1 & -0.574 & 0.819 & 0 & 0 & 0 \end{bmatrix} \\ S- &= \begin{bmatrix} 1 & 0.574 & -0.819 & 0 & 0 & 0 \end{bmatrix} \\ SW &= \begin{bmatrix} -2 & 0 & 0 & 0 & 0 & 0 \end{bmatrix} \\ BC &= \begin{bmatrix} 0 & 0 & 0 & 0 & 0 & 0 \end{bmatrix} \end{aligned}$$

where $S+$ is the sensitivity matrix for perturbations of the siderostat node on the $+x$ -axis, $S-$ is the sensitivity matrix for perturbations of the siderostat node on the $-x$ -axis, SW is the sensitivity matrix for perturbations of the switching mirror node, and BC is the sensitivity matrix for perturbations of the beam combiner node.

The optical sensitivity matrices for external OPD error are:

$$\begin{aligned} S+ &= \begin{bmatrix} 0 & -0.574 & 0.819 & 0 & 0 & 0 \end{bmatrix} \\ S- &= \begin{bmatrix} 0 & 0.574 & -0.819 & 0 & 0 & 0 \end{bmatrix} \\ SW &= \begin{bmatrix} 0 & 0 & 0 & 0 & 0 & 0 \end{bmatrix} \\ BC &= \begin{bmatrix} 0 & 0 & 0 & 0 & 0 & 0 \end{bmatrix} \end{aligned}$$

where $S+$, $S-$, SW , and BC are sensitivity matrices for perturbations of the same set of optical elements as defined above.

The optical sensitivity matrices for the internal OPD error are:

$$\begin{aligned} S+ &= \begin{bmatrix} 1 & 0 & 0 & 0 & 0 & 0 & 0 \end{bmatrix} \\ S- &= \begin{bmatrix} 1 & 0 & 0 & 0 & 0 & 0 & 0 \end{bmatrix} \\ SW &= \begin{bmatrix} -2 & 0 & 0 & 0 & 0 & 0 & 0 \end{bmatrix} \\ BC &= \begin{bmatrix} 0 & 0 & 0 & 0 & 0 & 0 & 0 \end{bmatrix} \end{aligned}$$

The linear optical model is combined with the state-space form of the structural finite element model to form the complete structural and optical model. This is done by using the perturbations of the nodes d as the output of the structural state space model and the input to the linear optical model.

Appendix 6: Output Performance Metric

This appendix contains a summary of the output performance metric and the SIM instrument operating modes relevant to the analyses contained in this memo. Further details on this topic may be found in [12].

SIM Operating Modes

Figure 15 is a block diagram of the open-loop interferometer model. A reaction wheel force disturbance, d , drives a structural-optical model of the spacecraft instrument, G_p , to produce physical pathlength output, y_{opd} . y_{opd} is the difference in pathlength, measured between a common wavefront external to the instrument and the beam combiner, traveled by light that enters at the two separate collecting apertures of the interferometer baseline. y_{opd} is represented as the sum of pathlength differences internal to the instrument, y_i (between the beam combiner and the collecting apertures) and pathlength differences external to the instrument, y_e (between the common wavefront and the collecting apertures). Either quantity may be quasistatic or dynamic.

The reaction wheel disturbance, d , in the block diagram represents a disturbance force (or torque) in only a single direction. Likewise, the transfer function of the structural plant, G_p , maps the contribution of that particular force or torque direction to the total OPD error. Since a reaction wheel contains disturbances in three force directions and two torque directions, the contributions of all these disturbances to the total OPD error is determined using linear superposition. The use of linear superposition requires the assumption that the input disturbances are uncorrelated, random disturbances. Although this assumption is not true for the reaction wheel disturbances, its use provides a conservative estimate of the total OPD error and therefore will be tolerated for this analysis. The analysis described in this memo is done in the frequency domain. $\Phi_{y_{OPD}}(w)$, the autospectrum of y_{opd} is related to $\Phi_{d_j}(w)$, the autospectrum of a disturbance force or torque in a particular direction by

$$\Phi_{y_{OPD}}(w) = \sum_{j=1}^n |G_{pj}(\omega)|^2 \Phi_{d_j}(w) \quad (2)$$

where $G_{pj}(\omega)$ is the transfer function of the structural plant relating the particular disturbance force or torque to OPD error. The total OPD error is the summation of the contribution of all force or torque components from all reaction wheels considered in the analysis.

In the sections that follow, additional blocks will be added to the open-loop interferometer model to represent the control action for the fringe acquisition and fringe tracking operating modes. Both OPD and WFT are optical output quantities of interest but only

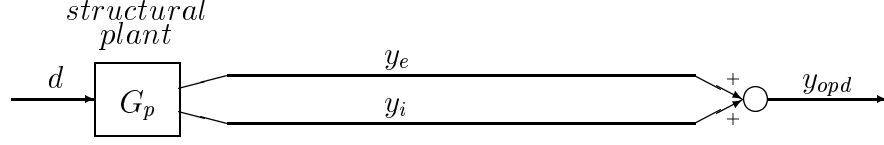


Figure 15: Block diagram of the open-loop interferometer model.

OPD will be considered here. Disturbance effects on WFT are considered in another memo by J. Melody [11].

Fringe Acquisition

Figure 16 illustrates a block diagram of the interferometer model for the Fringe Acquisition operating mode. In this operating mode the only control loop closed is the delay line control system. The reaction wheel disturbance, d , enters the integrated structure and optics model represented by G_p . The output of this model is split up into internal and external OPD, y_i and y_e . The internal OPD is assumed to be perfectly sensed by the internal metrology system and corrected by the optical delay line, represented here by its open loop plant, G_d and its compensator, K_d . Whatever internal OPD remains uncorrected is added to the uncorrected external OPD to produce the desired optical output quantity, stellar OPD or y_{opd} .

Now $\Phi_{y_{OPD}}(w)$, the autospectrum of y_{opd} is related to $\Phi_{d_j}(w)$, the autospectrum of a disturbance force or torque in a particular direction by

$$\Phi_{y_{OPD}}(w) = \sum_{j=1}^n |[G_{pj}(\omega)]_e + S_d[G_{pj}(\omega)]_i|^2 \Phi_{d_j}(w) \quad (3)$$

where $[G_{pj}(\omega)]_e$ is the transfer function of the structural plant relating the particular disturbance force or torque to external OPD error, $[G_{pj}(\omega)]_i$ is the transfer function of the structural plant relating the particular disturbance force or torque to internal OPD error, and S_d is the sensitivity function of the delay line as shown in the simplified block diagram of Figure 17.

$$S_d = \frac{1}{1 + K_d G_d} \quad (4)$$

Fringe Tracking

Figure 18 is the block diagram of the interferometer model that illustrates the fringe tracking mode. The structure is identical to that of the acquisition mode with the addition of an

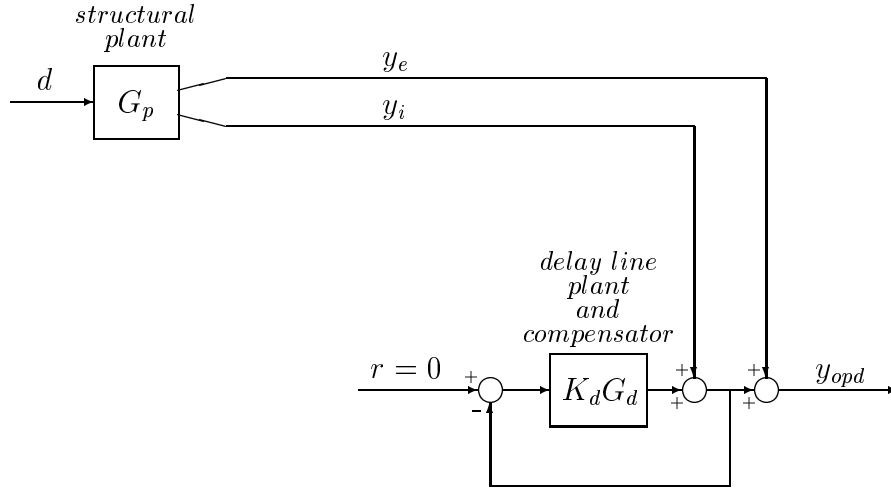


Figure 16: Block diagram of the interferometer model for fringe acquisition with OPD as the optical output quantity.

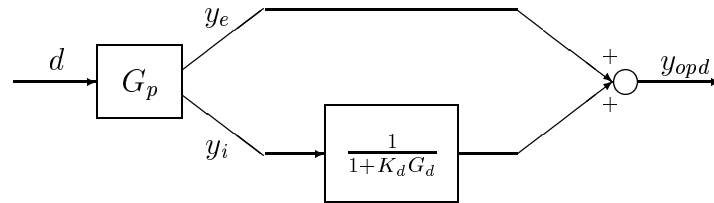


Figure 17: Simplified block diagram of fringe acquisition.

additional outer control loop, the fringe tracking loop. Physical OPD, y_{opd} , is measured by the location of an interference fringe on the CCD detector; the fringe displacement on the detector is proportional to y_{opd} . The CCD detector integrates over time T_c and signal m is the sampled mean during the intergration time T_c . The filter H_T is a continuous time approximation of the sampled mean process and is represented by the following equation.

$$H_T(\omega) = \text{sinc}\left(\frac{\omega T_c}{2}\right) \quad (5)$$

K_f is the fringe tracker compensator. The output of K_f is r , a servo command for the optical delay line, which will introduce an internal OPD, y_i , to offset the external OPD, y_e over the bandwidth of the delay line control loop.

For this case, $\Phi_{y_{OPD}}(w)$, is related to $\Phi_{dj}(w)$ by

$$\Phi_{y_{OPD}}(w) = \sum_{j=1}^n |S_f([G_{pj}(\omega)]_e + S_d[G_{pj}(\omega)]_i)|^2 \Phi_{dj}(w) \quad (6)$$

where S_f is the closed loop sensitivity function of the fringe tracker loop as shown in the simplified block diagram of Figure 19.

$$S_f = \frac{1}{1 + H_T K_f C_d} \quad (7)$$

where C_d is the complementary sensitivity function of the delay line.

$$C_d = 1 - S_d = \frac{K_d G_d}{1 + K_d G_d} \quad (8)$$

SIM Optical Performance Metric

The performance metric for both the fringe acquisition and fringe tracking modes of the interferometer is the fringe blur on the detector during the coherent integration time, T_c . The amount of blur depends on the stability of both OPD and DWT; only OPD will be considered here. Following the derivation of reference [5], $e_T(\tau, t)$, the OPD error during the integration time T_c is defined as the difference between the continuous time signal $y_{opd}(\tau)$ and its windowed mean, $m(t)$.

$$e_T(\tau, t) = y_{opd}(\tau) - m(t) \quad t \leq \tau \leq t + T_c \quad (9)$$

$\Phi_{e_T}(w)$, the autospectrum of the OPD error signal is related to $\Phi_{y_{OPD}}(w)$, the autospectrum of y_{opd} by

$$\Phi_{e_T}(w) = |S_T(w)|^2 \Phi_{y_{OPD}}(w) \quad (10)$$

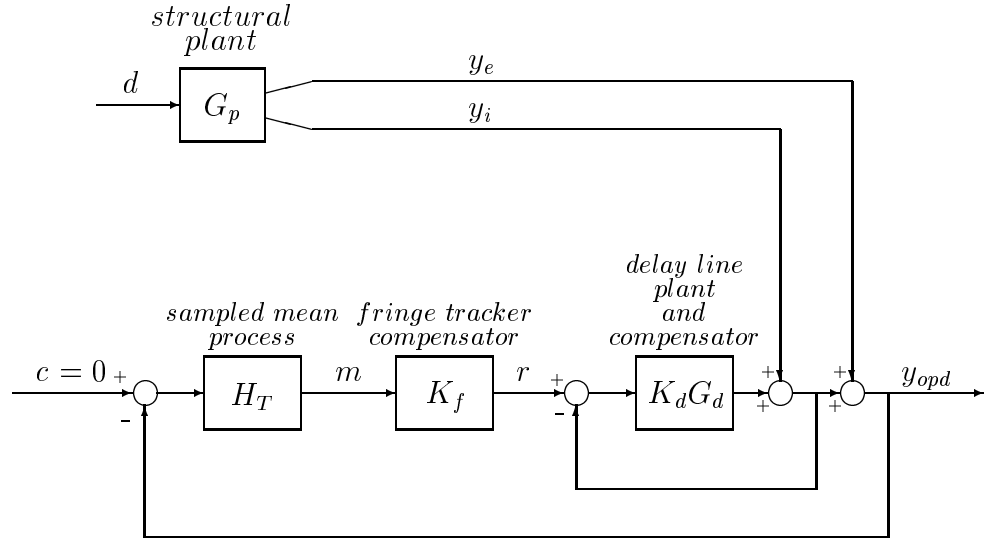


Figure 18: Block diagram of the interferometer model for fringe tracking with OPD as the optical output quantity.

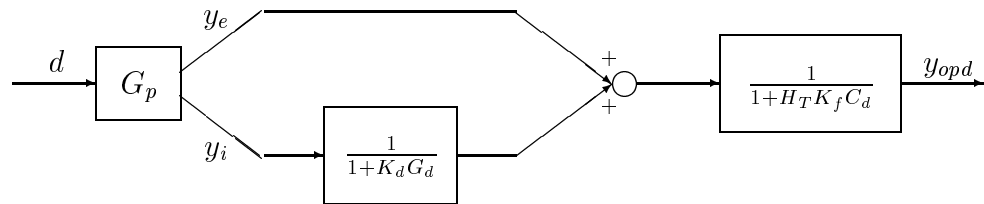


Figure 19: Simplified block diagram of fringe tracking.

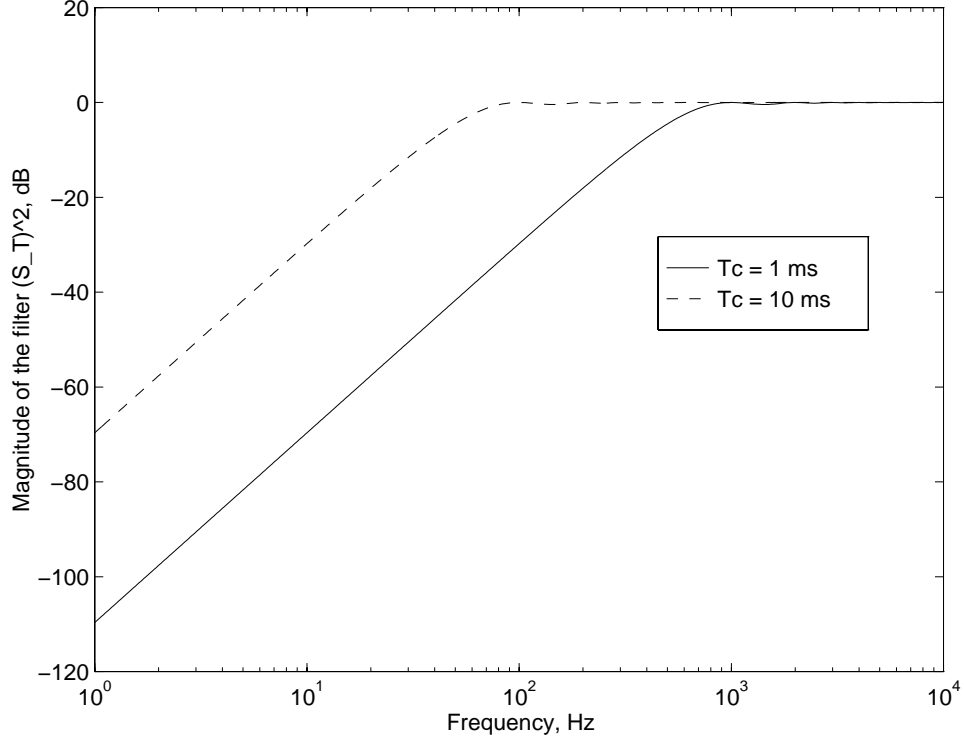


Figure 20: Comparison of the filter $|S_T(\omega)|^2$ for two different values of the integration time T_c .

where $|S_T(\omega)|^2$ is the high pass filter

$$|S_T(\omega)|^2 = 1 - \text{sinc}^2\left(\frac{\omega T_c}{2}\right) \quad (11)$$

$$= 1 - 2 \left[\frac{1 - \cos(\omega T_c)}{(\omega T_c)^2} \right] \quad (12)$$

Signals in y_{opd} which are below the sampling frequency $1/T_c$ are attenuated by this filter; the plot of the filter is shown in Figure 20. The performance metric, σ_{e_T} , is the RMS value of the fringe blur and its value can be directly compared to the requirements presented in the next section. The variance of the fringe blur, $\sigma_{e_T}^2$ is calculated using the following equation.

$$\sigma_{e_T}^2 = \frac{1}{2\pi} \int_{-\infty}^{\infty} |S_T(w)|^2 \Phi_{y_{OPD}}(w) dw \quad (13)$$

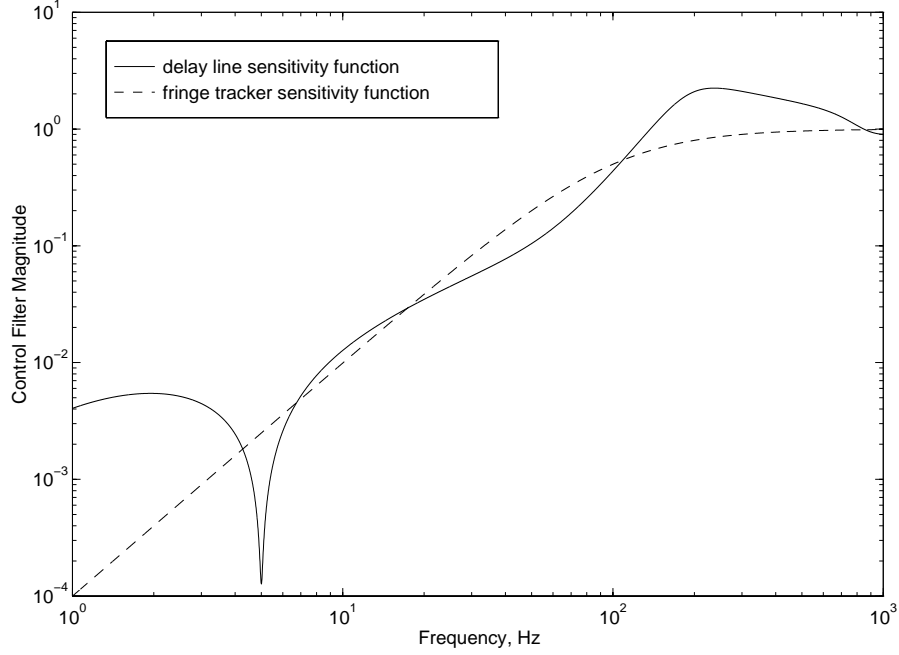


Figure 21: The delay line sensitivity function, S_d and the fringe tracker sensitivity function, S_f are applied as filters to model closed loop optical control.

Appendix 7: Closed Loop Synthesis

Filters are used to represent the effects of closed loop optical control. These filters are based on rules of thumb and experience with the components in testbeds such as MPI. The delay line sensitivity function is taken directly from the optical delay line control design by R. Grogan [15]. Figure 21 shows the filters used with Model v 0.0. Refer to Appendix 6 for block diagrams and equations describing the entire structure of the control system employing these control filters.

References

- [1] J. W. Yu, Personal communication, April, 1997.
- [2] S. S. Joshi, J. W. Melody, G. W. Neat, "Effects of Model Fidelity on Interferometer Design: A Case Study Using the Microprecision Interferometer, Final Results," JPL presentation, April 7, 1997, Draft version.
- [3] K. Smith, "Dynamic Analysis of the Mutually Orthogonal Hexapod Isolator, Status Report," JPL presentation, October 11, 1993.
- [4] J. Spanos, Z. Rahman, G. Blackwood, "A Soft 6-axis Active Vibration Isolator," American Control Conference, June 21, 1995.
- [5] S. W. Sirlin, A. M. San Martin, "A New Definition of Pointing Stability," JPL EM 343-1189, March 6, 1990.
- [6] M. Milman, *et al.*, "Integrated Modeling of Optical Systems User's Manual, Release 2.0," JPL D-13040, November 15, 1995.
- [7] M. Colavita, "Visibility and Phasing," JPL IOM, August 10, 1994.
- [8] G. Blackwood, T. Hyde, "Performance Definition and Control Loop Modelling for SITE," JPL IOM, September 9, 1994.
- [9] J. W. Melody, "ISIS Integrated Model and RCS Thruster Disturbance Analysis," JPL IOM 3411-96-174 ITP, May 20, 1996.
- [10] J. W. Melody, "Discrete-Frequency and Broadband Reaction Wheel Disturbance Models," JPL IOM 3411-95-200csi, June 1, 1995.
- [11] J. W. Melody, "SIM Wavefront Tilt Disturbance Analysis and Angle Feedforward," JPL IOM 3411-96-336 ITP, November 25, 1996.
- [12] L. Jandura, "SIM Optical Performance Metric for Optical Pathlength Difference," JPL IOM 352J-97-008, January 9, 1997.
- [13] G. W. Neat, J. W. Melody, "Hybrid Experimental/Analytical Performance Assessment Method to Establish Control Technology Readiness for Spaceborne Interferometry," JPL IOM 3413-96-138, April 23, 1996, paper submitted to em IEEE Transactions on Control Systems Technology.
- [14] J. W. Melody, Personal communication, November, 1996.
- [15] R. Grogan, Personal communication, December, 1996.